JOURNAL OF GUIDANCE, CONTROL, AND DYNAMICS
Vol. 15, No. 4, July-August 1992

Complicated Dynamics in Spacecraft Attitude Control Systems

George E. Piper*
General Electric Company, Princeton, New Jersey 08540
and
Harry G. Kwatny†
Drexel University, Philadelphia, Pennsylvania 19104

It is shown that a commonly used, momentum exchange, spacecraft attitude control configuration gives rise to complex nonlinear behavior involving multiple limit cycles and strange attractors. However, if the momentum wheel assembly performance parameters are adequately matched to the spacecraft, it is possible to achieve a globally stable equilibrium. The results are based on an analysis of a simple single-axis problem.

I. Introduction

DURING nominal operation, spacecraft require high pointing accuracies so that their payload may provide the desired coverage on the Earth's surface or other objects. Spacecraft attitude control is commonly provided by momentum exchange techniques. Typically, angular momentum is exchanged between a momentum wheel and the spacecraft body in response to the attitude error. For reliability, these control systems tend to be simple in their design. When attitude errors are small, the spacecraft dynamics are fairly linear and the spacecraft's behavior is well understood. Saturation, hysteresis, and time delays found in actuator dynamics are often ignored during analysis. Also, the control laws may contain nonlinearities, such as switching, which are intended to improve performance. In this paper, we will show how a linear single-input, single-output (SISO) control system containing nonlinear elements can give rise to such complicated behavior as multiple limit cycles, bifurcations, and strange attractors.

The system that we will be investigating is the pitch axis control system of a momentum-biased satellite. The pitch axis control system processes pitch angle information through a compensator that produces a wheel rate demand to the momentum wheel speed control loop. The compensator uses a simple variable-structure control scheme that is often used in spacecraft control systems. When the pitch error magnitude is smaller than a specified threshold, the compensator has a proportional plus integral structure. When the pitch error magnitude is larger than this threshold, the compensator has just a proportional structure. In concept, this provides better damping for large pitch errors and better pointing accuracy near the origin.

This pitch axis control system has been successfully flown on communication satellites for many years. However, as spacecraft increase in size, greater demands are placed on the control system actuators. Numerical simulations of the pitch axis control system on a hypothetical large satellite have revealed small, self-sustained oscillations about the operating point. These oscillations seem to be the result of the interaction between the variable-structure control law and the actuator control authority limitations. Standard limit cycle analysis, e.g., Ref. 1, fails to explain this oscillatory behavior and, hence, we have the motivation for this study.

Received Nov. 15, 1990; revision received Nov. 20, 1991; accepted for publication Nov. 27, 1991.

*Senior Member, Technical Staff, Astro Space Division.

†Raynes Professor of Mechanical Engineering, Mechanical Engineering & Mechanics Department.

II. Equations of Motion

Figure 1 shows a typical momentum-biased communication satellite configuration. The development of the pitch axis equation of motion follows the treatment in Refs. 2 and 3 for a rigid body with internal momentum wheel. Assuming small attitude errors and that the spacecraft's roll and yaw moments of inertia are equal, the pitch axis motion is uncoupled from the other axes and can be written as

$$T_d = I_z\ddot{\theta} + \dot{h}_w \tag{1}$$

where θ is the spacecraft pitch angle, I_z the pitch axis moment of inertia, h_w the wheel momentum, and T_d the external torque due to environmental disturbances and thruster firings.

The wheel momentum is regulated by the command torque that is defined as

$$T = (h_{\text{sys}} - h_w + h_c)/\tau \tag{2}$$

where h_{sys} is the nominal system momentum, h_c the output of the pitch axis control compensation, and τ the motor time constant. The momentum wheel motor has a limited torque capability, which is represented by a saturation function. The model for the momentum wheel is

$$\dot{h}_w = f(T, T_{\max}) \tag{3}$$

where

$$f(T,T_{\max}) = \begin{cases} T_{\max} & T > T_{\max} \\ T & -T_{\max} \le T \le T_{\max} \\ -T_{\max} & T < -T_{\max} \end{cases} \tag{4}$$

The pitch axis control compensation utilizes pitch angle information from an Earth sensor and an integrator as follows:

$$h_c = K_P\theta + K_I Y \tag{5}$$

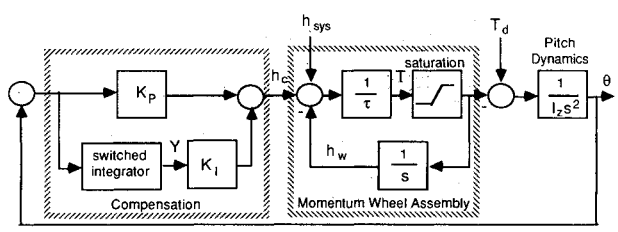

Fig. 1 Pitch axis control block diagram.

where K_P and K_I are the proportional and integrator gains, respectively, and Y is the integrator output. The integrator integrates the pitch error when the pitch error is less than a specified value θ_{th}. When the pitch error is greater than θ_{th}, the integrator is reset to zero. The model for the integrator is

$$\dot{Y} = g(Y,\theta,\theta_{th}) \tag{6}$$

$$g(Y,\theta,\theta_{th}) = \begin{cases} -\alpha Y & \theta > \theta_{th} \\ \theta & -\theta_{th} \le \theta \le \theta_{th} \\ -\alpha Y & \theta < \theta_{th} \end{cases} \tag{7}$$

Ideally, $\alpha \to \infty$ so the integrator resets to zero instantly. A block diagram of the pitch axis control system is shown in Fig. 1. All of the simulations to be described employ an ideal integrator reset where the integrator is reset to zero instantly when θ exceeds the threshold. The integrator was implemented as

$$\begin{aligned} \dot{Y} &= \theta, \quad \text{if} \quad |\theta| < \theta_{th} \\ \dot{Y} &= 0,\ Y = 0, \quad \text{if} \quad |\theta| \ge \theta_{th} \end{aligned} \tag{8}$$

Assuming that there are no external disturbances acting on the system (i.e., $T_d = 0$), the total momentum of the spacecraft will be h_{sys}. Integrating Eq. (1) yields

$$h_{sys} = I_z\dot{\theta} + h_w \tag{9}$$

which can be substituted into the system equations to eliminate the wheel momentum h_w, thus reducing the system to third order. The reduced system equations are

$$\dot{\omega} = -f(T,T_{max})/I_z, \qquad T = (I_z\omega + K_P\theta + K_I Y)/\tau \tag{10}$$

$$\dot{\theta} = \omega \tag{11}$$

$$\dot{Y} = g(Y,\theta,\theta_{th}) \tag{12}$$

The reduced system equations have one equilibrium point at the origin:

$$(\omega^*,\theta^*,Y^*) = (0,0,0) \tag{13}$$

Specific parameter values used in this analysis are listed in Table 1.

III. Preliminary Investigation

Initially, Eqs. (9-12) were numerically integrated with a Runge-Kutta integration method using the parameter values listed in Table 1. The results of the numerical integration revealed unusual oscillatory behavior. Figure 2 shows how the system responds to a large initial pitch error. The observed oscillations have a frequency of 0.041 rad/s. Note also that the long-term behavior of this oscillation is not established by these computational results. It is unclear if the oscillation will eventually diminish as suggested by the amplitude reduction near 3000 s or if it is actually quasiperiodic with a second frequency producing amplitude modulation. Figure 3 shows how the system responds to a small pitch error. As can be seen, the pitch error returns to the origin without any superfluous oscillations. The simultaneous presence of a stable equilibrium point and a stable limit cycle indicate that other limit sets must also exist. In the following paragraphs, we identify all of the limit sets and study their interaction as a function of key parameters. This analysis allows us to resolve the uncertainty with respect to long-term behavior.

We note that these observations were initially made with respect to a much more complete simulation model, which included multiaxis control and various additional details. Our initial effort focused on identifying a simple model that would reproduce that behavior in order to isolate the essential issues.

Table 1 Assumed satellite system parameter values

I_z	Pitch axis moment of inertia	9631.0	in.-lb-s^2
T_{max}	Maximum motor torque	1.0	in.-lb
τ	Motor time constant	23.0	s
K_P	Proportional compensation gain	697.0	in.-lb-s/rad
K_I	Integral compensation gain	17.425	in.-lb-s/rad-s
θ_{th}	Integrator reset threshold	0.0873	rad

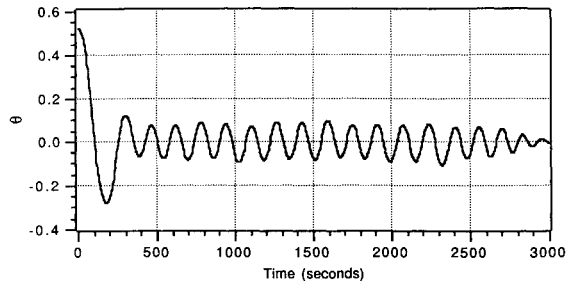

Fig. 2 Pitch axis control system's response to a large initial pitch error.

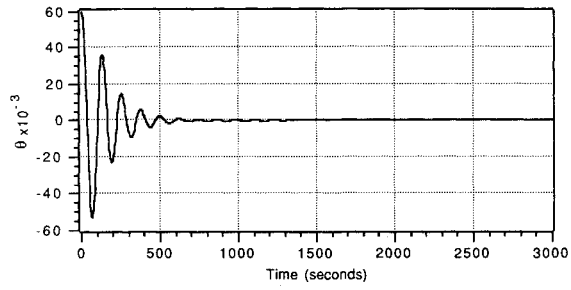

Fig. 3 Pitch axis control system's response to a small initial pitch error.

IV. Local Analysis

We will begin our analysis by performing a parametric study for trajectories confined to a neighborhood of the origin. It is assumed that $|\theta(t)| < \theta_{th}$, so that the integrator is in operation. Therefore, we ignore the integrator reset for this local analysis and replace Eq. (12) by

$$\dot{Y} = \theta \tag{14}$$

Identifying a Bifurcation Parameter

The Hopf bifurcation theorem characterizes the birth of a limit cycle from an equilibrium point as a parameter is varied through a critical value. In order for a Hopf bifurcation to occur, a single pair of complex conjugate eigenvalues of the linearized system must cross the imaginary axis transversely as a system parameter is varied. This motivates us to express the linearized dynamics of the pitch control system in matrix form

$$\begin{bmatrix} \dot{\omega} \\ \dot{\theta} \\ \dot{Y} \end{bmatrix} = \begin{bmatrix} -\frac{1}{\tau} & -\frac{K_P}{I_z\tau} & -\frac{K_I}{I_z\tau} \\ 1 & 0 & 0 \\ 0 & 1 & 0 \end{bmatrix} \begin{bmatrix} \omega \\ \theta \\ Y \end{bmatrix} \tag{15}$$

and to vary the three independent system parameters $1/\tau$, K_P/I_z, and K_I/I_z to produce a locus of the system eigenvalues.

The eigenvalue locus with respect to K_P/I_z does not cross the imaginary axis transversely. Although the eigenvalue locus

with respect to K_I/I_z does cross the imaginary axis, it crosses at $\omega = 0.0561$ rad/s, which is higher than the frequency of the oscillations observed in the initial investigation. The eigenvalue locus with respect to $1/\tau$ indicates a transversal intersection with the imaginary axis at $\omega = 0.0425$ rad/s, which is reasonably close to the frequency of the oscillations observed in the initial investigation. Thus, $1/\tau$ is a good candidate to use as the bifurcation parameter in our analysis. Therefore, we define $\mu = 1/\tau$.

Frequency-Domain Analysis

Simple frequency-domain calculations allow us to determine the existence and stability characteristics of a limit cycle. We first assume that the saturation function $f(T, T_{max})$ can be replaced by a sufficiently smooth function $f(T)$ and rewrite the system equations (9–11) and (14) in the first-order form

$$\dot{x} = Ax + Bf(\mu Cx) \tag{16}$$

where

$$x = \begin{bmatrix} \omega \\ \theta \\ Y \end{bmatrix}$$

$$A = \begin{bmatrix} 0 & 0 & 0 \\ 1 & 0 & 0 \\ 0 & 1 & 0 \end{bmatrix}, \qquad B = \begin{bmatrix} -\frac{1}{I_z} \\ 0 \\ 0 \end{bmatrix}, \qquad C = [I_z \; K_P \; K_I]$$

Equation (16) can be formulated into infinitely many equivalent feedback representations by introducing an arbitrary 1×1 matrix R as follows:

$$\dot{x} = Ax + BRy + B[f(\mu y) - Ry], \qquad y = Cx \tag{17}$$

Taking the Laplace transform of both sides of Eq. (17) and solving $\mathcal{L}(x)$ as a function of the Laplace variable s, then writing $e = -Cx$, we obtain

$$\mathcal{L}(e) = -G(s)\mathcal{L}(u) \tag{18a}$$

where

$$G(s) = C[sI - (A + BRC)]^{-1}B \tag{18b}$$

$$u = h(e;\mu) := -f(\mu e) + Re \tag{18c}$$

Equations (18) define a continuum of equivalent nonlinear multiple-loop feedback representations that have been separated into a dynamical linear part with a transfer matrix $G(s)$ and a memoryless nonlinear part $h(e;\mu)$. Because $h(0;\mu) = 0$, the system has an equilibrium point $x = 0$ (corresponding to $e = 0$).

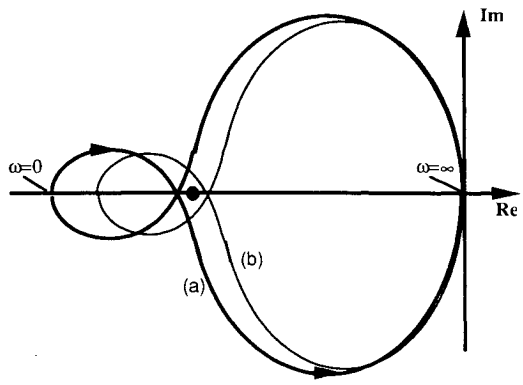

Fig. 4 Characteristic locus of $G(s)J(\mu)$, where the dot identifies the critical point: a) $\mu > K_I/K_P$ (stability); b) $\mu = K_I/K_P$ (instability).

To avoid singularities at $s = 0$, we choose $R = -1$, which gives us

$$G(s) = \frac{-s^2 - (K_P/I_z)s - (K_I/I_z)}{s^3 - s^2 - (K_P/I_z)s - (K_I/I_z)} \tag{19a}$$

$$h(e;\mu) = -f(\mu e) - e \tag{19b}$$

The Jacobian $J = D_e h(0;\mu)$ is

$$J = -\mu - 1 \tag{20}$$

thus,

$$G(s)J(\mu) = (\mu + 1)\frac{s^2 + (K_P/I_z)s + (K_I/I_z)}{s^3 - s^2 - (K_P/I_z)s - (K_I/I_z)} \tag{21}$$

The Nyquist stability criterion states that the closed-loop system has a stable equilibrium point $x = 0$ if and only if the number of counterclockwise encirclements of the critical point $(-1 + j0)$ by the characteristic loci of the open-loop transfer matrix $G(s)J(\mu)$ is equal to the number of open-loop poles in the right half-plane.[4] The open-loop transfer function $G(s)J(\mu)$ given by Eq. (21) has poles at

$$s = 1.0693, \; -0.0346 \pm 0.0222j$$

Since $G(s)J(\mu)$ has one positive real pole, the characteristic loci must encircle the point $(-1 + j0)$ in the counterclockwise direction once to indicate that the system is stable. Figure 6 shows the characteristic loci of $G(s)J(\mu)$ for two different values of μ. For $\mu < K_I/K_P$, the loci encircles the $-1 + j0$ point once, but in the clockwise direction, which indicates that the system is unstable. The characteristic loci for the bifurcation value $\mu_0 = K_I/K_P$ passes through the $-1 + j0$ point, indicating criticality and where we have $G(j\omega_0)J(\mu_0) = -1$ with $\omega_0 \neq 0$. Figure 4 also shows the characteristic for $\mu > K_I/K_P$. The loci encircles the $-1 + j0$ point once in the counterclockwise direction, indicating that the system is stable. The stability analysis indicates that a pair of complex conjugate roots cross the imaginary axis transversally at $\mu = \mu_0$, thereby suggesting a Hopf bifurcation. To investigate this further, we use the frequency domain version of the Hopf bifurcation theorem.[5] The derivation of this result combines harmonic balance approximation, similar to describing function analysis,[1] with the small-amplitude assumption that underlies the conventional Hopf bifurcation theorem. Thus, it provides a describing functionlike analysis that rigorously predicts the existence of a limit cycle along with its stability. The price paid for rigor is that the nonlinearity must be sufficiently smooth. Let us summarize the main ideas specialized to the case of interest here: $f(\cdot)$ is a scalar valued and symmetric function of a scalar variable. We assume that μ is close to, but not equal to μ_0 and denote by $\lambda(j\omega)$ the characteristic function of $G(j\omega)J(\mu)$, which intersects the real axis near the point $-1 + j0$, the intersection occurring at $\omega = \omega_r$. Now define the complex valued function

$$\zeta(\omega_r) = (1/8)G(j\omega_r)f'''(\mu e^*)$$

where $f'''(\mu e^*)$ is the third derivative of $f(\cdot)$ evaluated at the equilibrium point. Suppose f in Eq. (16) is C^4, $\zeta(\omega_r)$ is nonzero, and the half-line $-1 + \alpha^2\zeta(\omega_r)$, α real and ≥ 0, intersects the curve $\lambda(j\omega)$ transversally at a point P'. Then there exists a unique periodic orbit in a neighborhood of the equilibrium point. The periodic orbit is the unique attractor in this neigh-

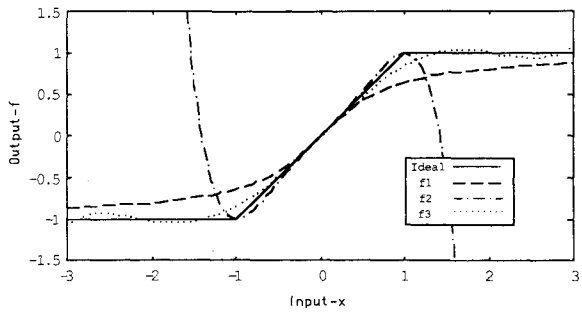

Fig. 5 Smooth approximations of the saturation function.

borhood if the following encirclement condition holds: the total number of counterclockwise encirclements of the point $P' + \delta\zeta(\omega_r)$, $\delta > 0$ arbitrarily small, by the characteristic loci λ is equal to the number of poles of $\lambda(s)$ with positive real part.

The frequency domain Hopf bifurcation theorem requires the nonlinear function to be C^4 jointly in μ and e (i.e., the function must have four continuous derivatives). Since the function $f(\mu e)$ is only piecewise continuous, we must replace it by a sufficiently smooth function. Three smooth approximations for $f(\mu e)$ were developed. The first approximation for $f(\mu e)$ is given by

$$f_1(\mu e) = \frac{2}{\pi} T_{\max} \arctan\left(\frac{\pi \mu e}{2 T_{\max}}\right) \tag{22}$$

where $f(\mu e) \to \pm T_{\max}$ as $\mu e \to \pm\infty$, and where $f'(0) = 1$. The second approximation for $f(\mu e)$ is a fifth-order polynomial that satisfies the conditions:

$$f(T_{\max}) = T_{\max}, \qquad f'(T_{\max}) = 0$$

$$f(0) = 0, \qquad f'(0) = 1$$

$$f(-T_{\max}) = -T_{\max}, \qquad f'(-T_{\max}) = 0$$

which gives

$$f_2(\mu e) = \mu e + \frac{(\mu e)^3}{2T_{\max}^2} - \frac{(\mu e)^5}{2T_{\max}^4} \tag{23}$$

The third smooth approximate for $f(\mu e)$ was derived numerically. Replacing $T_{\max}$ by its numerical value listed in Table 1, a fifth-order polynomial was least squares fit to data points on the $f(\mu e)$ curve. The weighting of the data points was increased near the origin and at $|\mu e| > T_{\max}$. The resulting approximation is given by

$$f_3(\mu e) = \mu e - 0.1650(\mu e)^3 + 0.0103(\mu e)^5 \tag{24}$$

The smooth approximations for $f(\mu e)$ are shown in Fig. 5.

$$f_1(x) = \frac{2}{\pi} \arctan\left(\frac{\pi}{2} x\right)$$

$$f_2(x) = x + \frac{1}{2}x^3 - \frac{1}{2}x^5$$

$$f_3(x) = x - 0.1650x^3 + 0.0103x^5$$

The correction vector ζ was calculated for each of the $f(\mu e)$ approximations. Since Im $\lambda(j\omega) = 0$ when $\omega = \pm\sqrt{K_I/I_z}$, we identify $\omega_r = \sqrt{K_I/I_z}$. Moreover, $\lambda(j\omega) = -1$ when $\omega = \sqrt{K_I/I_z}$ and $\mu = K_I/K_P$, thus criticality occurs at $\omega_0 = \sqrt{K_I/I_z}$ and $\mu_0 = K_I/K_P$. The correction vector is computed to be

$$\zeta(\omega_r) = \frac{K_P}{8\,(K_P + K_I)} f'''(0) \tag{25}$$

Observe that $\zeta(\omega_r)$ is a real number whose sign depends on the third derivative of the $f(\mu e)$ approximation. Hence, the vector from -1 in the direction $\zeta(\omega_r)$ lies on the real axis in the Nyquist plots and its direction depends on the sign of $f'''(0)$. The third derivatives of the smooth approximations are

$$f_1'''(0) = -\frac{\pi^2}{2T_{\max}^2}\mu^3$$

$$f_2'''(0) = \frac{3}{T_{\max}^2}\mu^3$$

$$f_3'''(0) = -0.9900\,\mu^3$$

f_1''' and f_3''' have negative signs so that $\zeta(\omega_r)$ will point toward the left. Referring to Fig. 4, $\zeta(\omega_r)$ will only intersect the characteristic loci when $\mu > K_I/K_P$ and the equilibrium is stable. The frequency-domain Hopf bifurcation theorem asserts that the system will have an unstable limit cycle when $\mu > K_I/K_P$. On the other hand, f_2''' has a positive sign, and $\zeta(\omega_r)$ will point toward the right. Again, with reference to Fig. 4, $\zeta(\omega_r)$ will only intersect the characteristic loci when $\mu < K_I/K_P$ and the equilibrium is unstable. This implies that the system will have a stable limit cycle when $\mu < K_I/K_P$.

However, upon inspecting Fig. 5, it is obvious that f_2 is a poor approximation of f over the critical region. Therefore, we disregard the results predicted with this approximation. The issue of approximation of a nonsmooth nonlinearity in order to apply the theorem is subtle and important, which is why we include the example of f_2. One could argue, of course, that saturation should be modeled by a smooth function to begin with. Computer simulations confirm the existence of an unstable limit cycle for $\mu > K_I/K_P$.

Poincaré Mapping

To verify our analysis, the local system equations (9-11) and (14) were integrated using a Runge-Kutta method with a fixed step size of 0.1 s. The simulation results were analyzed using Poincaré mapping techniques as discussed in Refs. 6 and 7 to gain better insight into the system behavior. The Poincaré map condenses the behavior of the three-dimensional trajectories to a mapping of a two-dimensional surface onto itself. Thus, the stability properties of the map reflect the stability properties of the flow. Poincaré sections were generated by plotting the points where the trajectory intersects the $(\theta > 0, Y)$ plane. Upon inspecting the Poincaré section, we observe a sequence of dots generated by the so-called Poincaré mapping. Transient motions appear as scattered dots representing an orbit of the map in the two-dimensional surface. Periodic trajectories (of order n) are observed as a systematic repetitive sequence of n fixed mapping points.

Phase diagrams were produced by plotting the maps for different initial values on the same Poincaré section. These

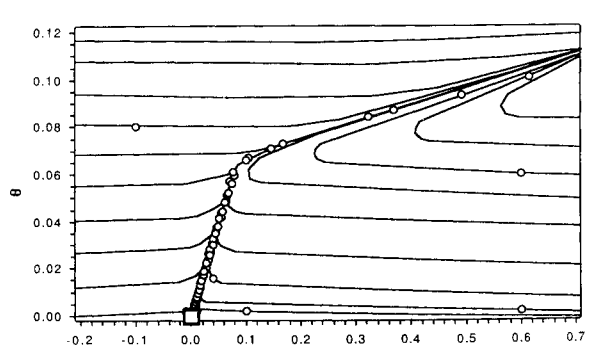

Fig. 6 Poincaré section of the pitch axis control system without the integrator reset for $\mu = 0.022$ (illustrates instability of equilibrium prior to bifurcation): □ = unstable origin; O = data points.

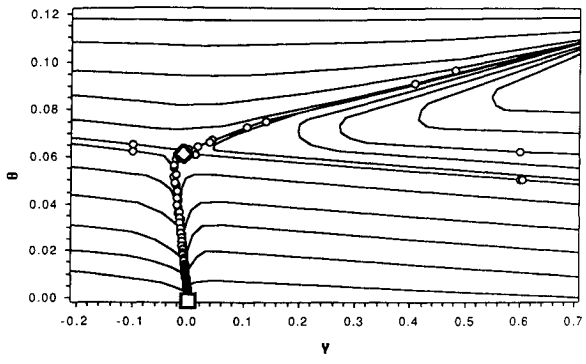

Fig. 7 Poincaré section of the pitch axis control system without the integrator reset for $\mu = 0.026$ (illustrates the birth of an unstable limit cycle following bifurcation): □ = stable origin; ◇ = unstable limit cycle; O = data points.

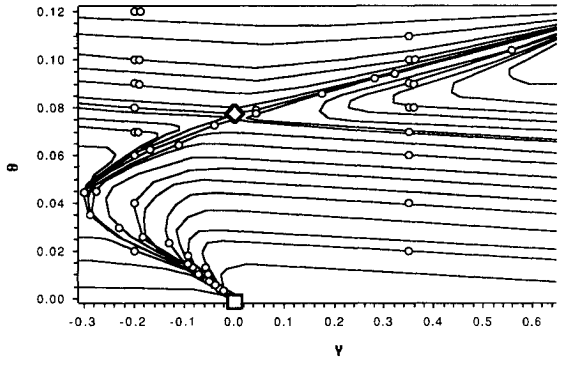

Fig. 8 Poincaré section of the pitch axis control system without the integrator reset for $\mu = 0.050$ (illustrates continual growth of the unstable limit cycle amplitude as μ is increased): □ = stable origin; ◇ = unstable limit cycle; O = data points.

phase diagrams are shown in Figs. 6–8. The intersection of the trajectories with the Poincaré section are represented by small circles. The lines connecting the circles help to organize the picture. These lines connect points on the same orbit. Otherwise, their shape is only meant to be suggestive. In some instances, it is possible to define a continuous flow on the section that approximates the discrete orbits, as described in Ref. 6. That has not been done here. The Poincaré section in Fig. 6 illustrates the system behavior prior to bifurcation when $\mu < \mu_0$. The equilibrium (depicted by the large square) is unstable and behaves like a saddle point in the Poincaré section. The stable manifold lies on the Y axis, and the unstable manifold runs off in the ± 0 directions.

The Poincaré section in Fig. 7 reveals the presence of an unstable limit cycle and a stable equilibrium following bifurcation when $\mu > \mu_0$. The unstable limit cycle is depicted by the large diamond and behaves like a saddle point in the Poincaré section. Its stable manifold runs horizontally, almost parallel to the Y axis, and its unstable manifold runs somewhat vertically. Figure 8 illustrates how the amplitude of the unstable limit cycle grows as μ is increased.

V. Global Analysis

To study the global behavior of the system, the effects of the integrator reset must be considered. Therefore, Eq. (12) was included for the global analysis. The system equations (9–12) were integrated using the same fixed step size Runge-Kutta method as in the local analysis.

Numerical Simulation: Bifurcation Picture

Simulations revealed the presence of two stable limit cycles symmetrically located about an unstable equilibrium $\mu < \mu_0$. Figure 9 shows the projection of these cycles on to the θ-ω plane. Note that the dynamical equations (10–12) or (10), (11), and (8) possess a symmetry, i.e., the equations are invariant under the change of coordinates $(\omega, \theta, Y) \rightarrow (-\omega, -\theta, -Y)$. Figure 9 clearly shows that the two limit cycles inherit this symmetry. The other two projections, which are not included here, also reveal this symmetry. As μ was increased past μ_0, an unstable limit cycle bifurcated from equilibrium as described in the local analysis. Also, the two stable limit cycles moved closer together. As we continued to increase μ, the two stable limit cycles experienced a period doubling bifurcation while moving still closer together. Figure 10 shows the projections of the stable cycles following the period doubling bifurcation. As μ was increased further, the two stable limit cycles bump into each other and combine into a single stable limit cycle with two subharmonics. Figure 11 shows the projections of the limit cycle with two subharmonics. Continuing to increase μ caused the cycle to become aperiodic and behave chaotically, which is shown in Fig. 12. Finally, μ was increased to the point where the amplitude of unstable limit cycle grew large enough to collide with the strange attractor and they were both annihilated, leaving a globally stable equilibrium. A bifurcation diagram depicting max $|\theta|$ vs μ is shown in Fig. 13. The bifurcation diagram summarizes the results of the parametric study. The trajectories in Figs. 3 and 4 correspond to a parameter value slightly larger than the critical value at which annihila-

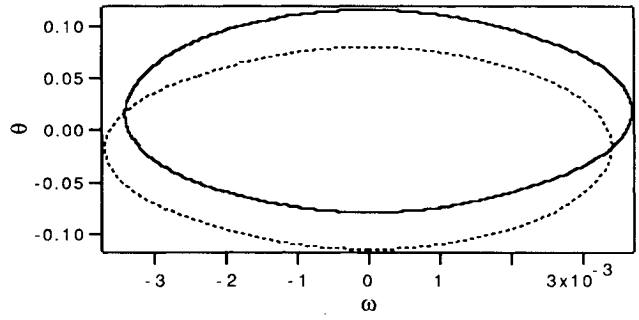

Fig. 9 Two stable limit cycles at $\mu = 0.020$.

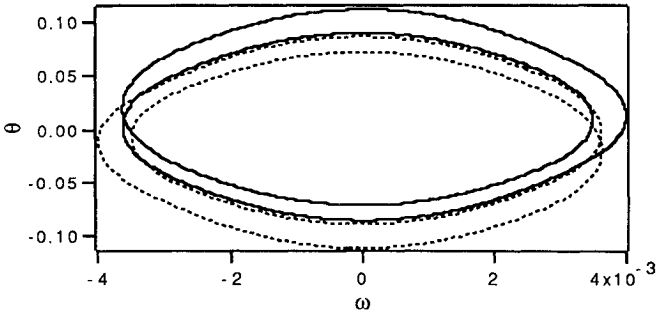

Fig. 10 Two stable limit cycles following period doubling bifurcation at $\mu = 0.030$.

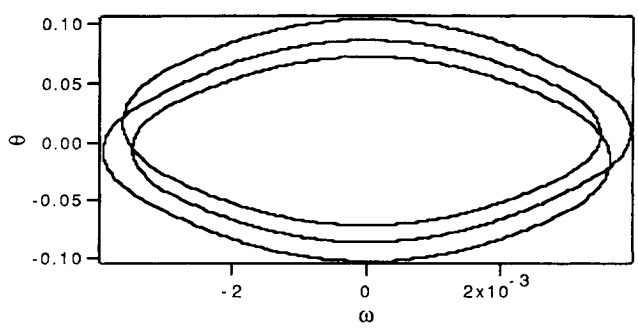

Fig. 11 Stable limit cycle following merging of the two stable limit cycles at $\mu = 0.033$.

tion of the strange attractor takes place. Thus, we see both trajectories eventually converging to the stable equilibrium. Nevertheless, we clearly see the "fingerprint" of the strange attractor in the large error response of Fig. 3. The trajectory appears to cycle as it slowly passes through the region in state space that was occupied by the strange attractor prior to its annihilation.

Grebogi et al.[6] have studied, in general terms, the behavioral changes that occur in dynamical systems when an unstable periodic trajectory collides with a coexisting chaotic attractor. They call such collisions "crises." As a result of their investigations, they conjecture that "almost all sudden changes in the size of chaotic attractors and almost all sudden destructions or creations of chaotic attractors are due to crises." Our observations in this instance are consistent with their conclusions.

Physically, as the momentum wheel's response becomes sluggish (i.e., the motor time constant becomes large), the system behavior becomes unfavorable. Although the integrator reset hinders the pitch error from becoming unbounded, small erratic oscillations can appear. This undesirable behavior is a theoretical possibility that has not, to our knowledge,

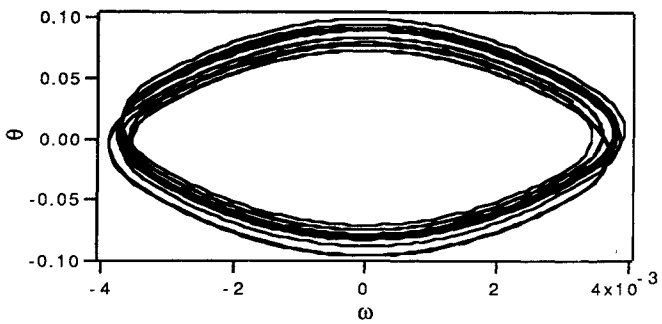

Fig. 12 Strange attractor at $\mu = 0.042$

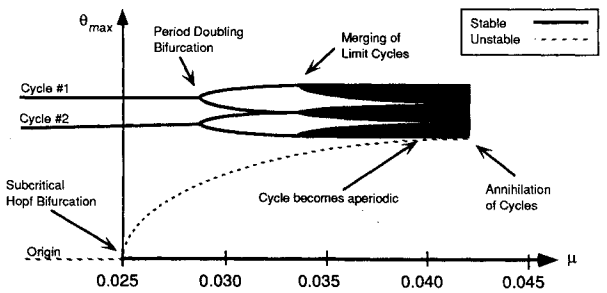

Fig. 13 Pitch axis control system bifurcation diagram.

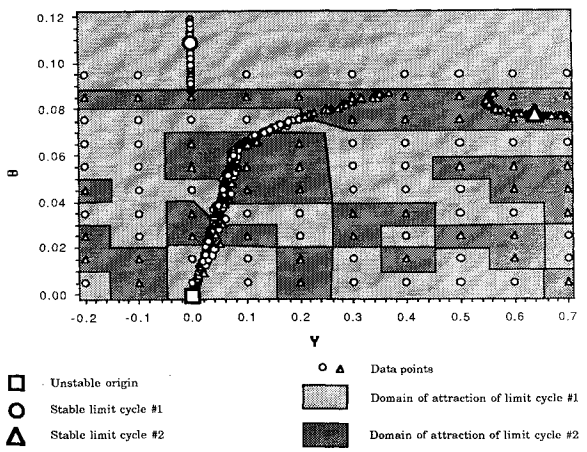

Fig. 14 Regions of attraction on the Poincaré section of the two stable limit cycles at $\mu = 0.022$.

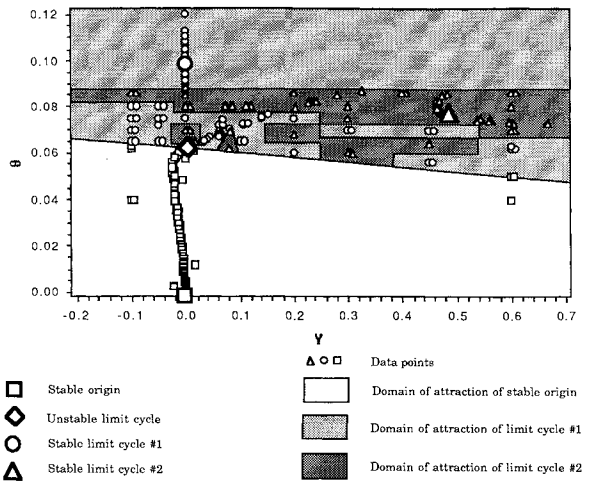

Fig. 15 Regions of attraction on the Poincaré section of the two stable limit cycles at $\mu = 0.026$, following the subcritical Hopf bifurcation.

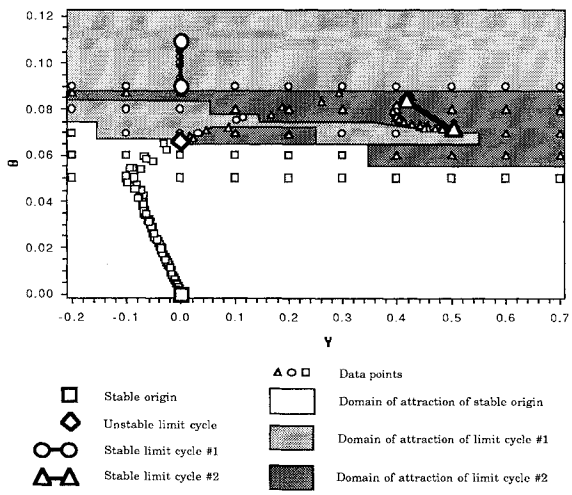

Fig. 16 Regions of attraction on the Poincaré section at $\mu = 0.030$, following the period doubling bifurcation of the two stable limit cycles.

been observed in actual spacecraft. The motor time constant is proportional to the momentum wheel moment of inertia. As spacecraft increase in size, larger momentum wheels will be needed. Momentum wheel motors with insufficient torque capabilities can cause these adverse effects even though the linear analysis predicts satisfactory performance.

Numerical Simulation: Regions of Attraction

With the coexistence of multiple attractors competing in the phase space of a single dynamical system, different initial conditions lead to different final states. To study the regions of attraction of these attractors, trajectories were labeled according to the attractor in which they terminated. The regions of attraction are illustrated on the Poincaré section shown in Figs. 14–19.

Figure 14 shows the regions of attraction for the two stable limit cycles prior to the Hopf bifurcation, $\mu < \mu_0$. The two stable limit cycles are depicted by a large circle and triangle. The equilibrium is depicted by a large square. The small circles and triangles represent the intersections of the trajectories with the Poincaré section and correspond to the attractor in which trajectory terminates. As you can see in the diagram, all trajectories intersecting the Poincaré section $\theta > 0.087$ (corresponding to θ_{th}) end up at limit cycle 1. Since the two stable limit cycles are symmetric, all trajectories intersecting the Poincaré section at $\theta < -0.087$ (corresponding to $-\theta_{th}$) end

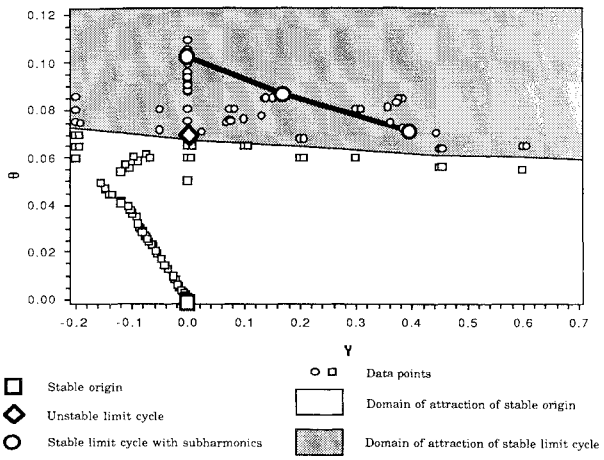

Fig. 17 Regions of attraction on the Poincaré section at $\mu = 0.033$, following the merging of the two stable limit cycles.

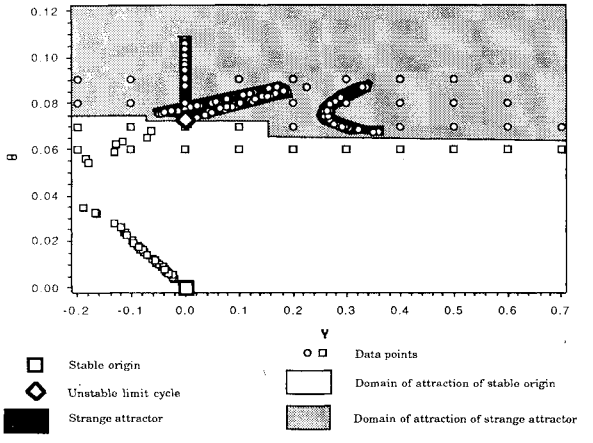

Fig. 18 Regions of attraction on the Poincaré section of the strange attractor and the origin at $\mu = 0.042$.

up at limit cycle 2. For trajectories intersecting the Poincaré section at $|\theta| < 0.087$, there is no distinct separatrix that defines the regions of attraction (with respect to the very coarse resolution of our calculations). The destination of the trajectories is highly sensitive to the trajectory's initial conditions—especially near the unstable manifold of the origin.

Figure 15 shows the regions of attraction for the two stable limit cycles and the equilibrium at $\mu = 0.024$, following the Hopf bifurcation. The small squares represent the trajectories that terminate at the equilibrium. The unstable limit cycle is depicted by a large diamond. The stable manifold of the unstable limit cycle clearly separates the equilibrium's region of attraction from the two stable limit cycle's region of attraction.

Figure 16 shows the regions of attraction for the two stable limit cycles and the equilibrium at $\mu = 0.030$, following the period doubling bifurcation. The two stable limit cycles with their subharmonics are represented by the large circles and triangles connected by a heavy line. As can be seen, the two stable limit cycles move closer together whereas the unstable limit cycle's amplitude increases. Again, even though our resolution is poor, it is clear that the stable manifold of the unstable limit cycle forms the boundary of the domain of attraction for the stable equilibrium.

Figure 17 shows the regions of attraction at $\mu = 0.033$, following the merging of the two stable limit cycles. The newly formed limit cycle with its subharmonics is represented by the three large circles connected by heavy lines. There are now only two attractors, the stable equilibrium point at the origin and the stable limit cycle.

As mentioned earlier, the stable attractor becomes aperiodic as μ is increased. Figure 18 shows the region of attraction for

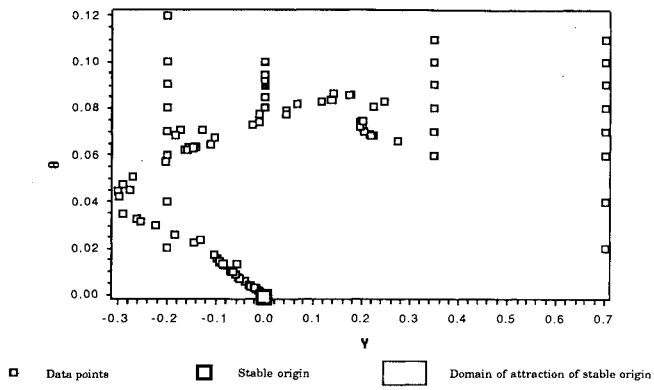

Fig. 19 Poincaré section following the annihilation of the strange attractor by collision with the unstable limit cycle at $\mu = 0.050$. The origin is a global attractor.

the strange attractor at $\mu = 0.042$. The black area on the Poincaré section represents the region in which the strange attractor exists. Trajectories enter this region but never leave. Note the proximity of the unstable limit cycle to the strange attractor.

Finally, Fig. 19 shows the equilibrium as a global attractor at $\mu = 0.050$ following the annihilation of the strange attractor with the unstable limit cycle.

VI. Conclusions

Unusual oscillatory behavior was observed during the routine simulation of a communications satellite equipped with a more or less conventional attitude control system. Because of the complicated nature of the self-sustained oscillations, it was necessary to combine analytical techniques with numerical simulation to unfold the system behavior. Modern concepts of dynamical systems theory and bifurcation analysis provided an essential guide to the structuring of the investigation and interpretation of the results. The analysis showed that by varying the motor time constant the pitch axis control system can be driven unstable. In the presence of torque saturation, the equilibrium loses stability via a subcritical Hopf bifurcation. This is important because the region of attraction of the stable equilibrium is constrained by an unstable limit cycle that shrinks as criticality is approached. The analysis also showed how a switching control law in the presence of torque saturation can cause a simple SISO system to exhibit complicated dynamical behavior. By varying the motor time constant, the birth and annihilation of multiple limit cycles can occur. These results fully explain the unusual behavior observed in initial simulations of a satellite and provide insights into the implications of design choices available to the engineer.

References

[1]Gelb, A., and Vender Velde, W. E., *Multiple-Input Describing Functions and Nonlinear System Design,* McGraw-HIll, New York, 1968.

[2]Agrawal, B. N., *Design of Geosynchronous Spacecraft,* Prentice-Hall, London, 1986.

[3]Kaplan, M. H., *Modern Spacecraft Dynamics and Control,* Wiley, New York, 1976.

[4]MacFarlane, A. G. J., and Postlethwaite, I., "The Generalized Nyquist Stability Criterion and Multivariable Root Locus," *International Journal of Control,* Vol. 25, No. 8, 1977, pp. 81–127.

[5]Mees, A., and Chua, L., "The Hopf Bifurcation Theorem and its Application to Nonlinear Oscillations in Circuits and Systems," *IEEE Transactions on Circuits and Systems,* Vol. CAS-26, No. 4, 1979, pp. 235–254.

[6]Guckenheimer, J., and Holmes, P., *Nonlinear Oscillations, Dynamical Systems and Bifurcations of Vector Fields,* Springer-Verlag, New York, 1983.

[7]Thompson, J., and Stewart, H., *Nonlinear Dynamics and Chaos,* New York, 1986.

[8]Grebogi, C., Ott, E., and Yorke, J. A., "Crises, Sudden Changes in Chaotic Attractors and Transient Chaos," *Physica,* Vol. 7D, No. 1, 1983, pp. 181–200.